R. A. Evarestov and A. Kuzmin,
Topological analysis of chemical bonding in the layered FePSe3 upon pressure-induced phase transitions,
J. Comput. Chem. 41 (2020) 2610-2623.

Topological analysis of chemical bonding in the layered $FePSe_3$ upon pressure-induced phase transitions

Robert A. Evarestov*and Alexei Kuzmin†

November 3, 2020

Abstract

Two pressure-induced phase transitions have been theoretically studied in the layered iron phosphorus triselenide ($FePSe_3$). Topological analysis of chemical bonding in $FePSe_3$ has been performed based on the results of first-principles calculations within the periodic linear combination of atomic orbitals (LCAO) method with hybrid Hartree-Fock-DFT B3LYP functional. The first transition at about 6 GPa is accompanied by the symmetry change from $R\bar{3}$ to $C2/m$, whereas the semiconductor-to-metal transition (SMT) occurs at about 13 GPa leading to the symmetry change from $C2/m$ to $P\bar{3}1m$. We found that the collapse of the band gap at about 13 GPa occurs due to changes in the electronic structure of $FePSe_3$ induced by relative displacements of phosphorus or selenium atoms along the c-axis direction under pressure. The results of the topological analysis of the electron density and its Laplacian demonstrate that the pressure changes not only the interatomic distances but also the bond nature between the intralayer and interlayer phosphorus atoms. The interlayer P–P interactions are absent in two non-metallic $FePSe_3$ phases while after SMT the intralayer P–P interactions weaken and the interlayer P–P interactions appear.

Keywords: $FePSe_3$, layered compound, topological analysis, high pressure, semiconductor-to-metal transition, first-principles calculations.

*Department of Quantum Chemistry, Saint Petersburg State University, 7/9 Universitetskaya Naberezhnaya, St. Petersburg 199034, Russian Federation; E-mail: r.evarestov@spbu.ru

†Institute of Solid State Physics, University of Latvia, Kengaraga street 8, LV-1063, Riga, Latvia; E-mail: a.kuzmin@cfi.lu.lv

R. A. Evarestov and A. Kuzmin,
Topological analysis of chemical bonding in the layered FePSe3 upon pressure-induced phase transitions,
J. Comput. Chem. 41 (2020) 2610-2623.

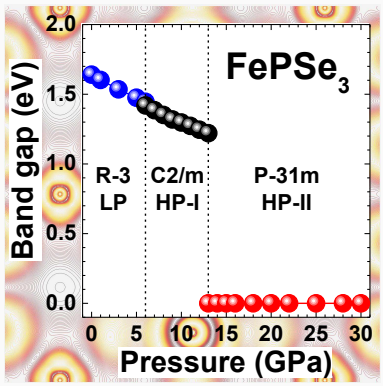

Pressure-induced phase transitions in iron phosphorus triselenide ($FePSe_3$) were studied using first-principles calculations and the topological analysis of the electron density and its Laplacian. The calculations predict the semiconductor-to-metal transition (SMT) at ∼13 GPa. The origin of the SMT is attributed to the pressure-induced changes in the $FePSe_3$ electronic structure caused by the relative displacement of phosphorus or selenium atoms along the *c*-axis direction. The pressure strongly affects both the interatomic distances and the bond nature between the intralayer and interlayer phosphorus atoms.

1 INTRODUCTION

Topological analysis of the electron density distribution in materials is an efficient method of obtaining information about the existence and nature of chemical bonds.[1,2] Due to the progress in quantum chemistry calculations, the method has gained popularity and finds numerous applications in studies of organic and inorganic compounds.[3–15] In particular, the method helps to identify changes in chemical bonds and mechanisms of phase transitions under high pressure.[16–26] At the same time, the use of topological analysis for the understanding of bonding in layered compounds is not numerous. Recently it was successfully employed to evidence peculiarities of chemical bonding in layered TiS_2 crystals using the analysis of the electron density, obtained from synchrotron X-ray diffraction data and density functional theory calculations.[27] The method was also used to study the evolution of chemical bonding during solid-state $D_{3h} \rightarrow D_{3d}$ reaction in monolayered TiS_2.[28]

In this study, we apply the topological analysis to probe in detail both intralayer and interlayer interactions between atoms being responsible for the recently found[29] pressure-induced semiconductor-to-metal (SMT) transition in iron phosphorus triselenide ($FePSe_3$).

Bulk $FePSe_3$ is a layered magnetic semiconductor with the narrow optical indirect band gap of 1.3 eV[30] and possesses intrinsic antiferromagnetism below the Néel temperature of about 112-123 K.[31–33] The magnetism is caused by a high-spin state of Fe^{2+} ions (d^6) ordered on a honeycomb lattice with the total spin projection $S = 2$ and the magnetic moments $m_0 = 4.9\mu_B$.[32,33] The weak van der Waals (vdW) interactions between neighbouring layers in $FePSe_3$ make its structure and properties strongly pressure dependent. The application of high pressure induces the high-to-low spin-state transition of Fe^{2+} ions, thus producing a nonmagnetic $FePSe_3$ phase through the pressure-induced spin-quenching ($S = 0$).[29,34] Moreover, it was discovered recently that abrupt spin-crossover is accompanied by SMT and the appearance of a superconducting state with a transition temperature $T_C \sim 2.5$ K at 9 GPa and the maximum $T_C \sim 5.5$ K at about 30 GPa.[29]

Besides, $FePSe_3$ demonstrates enhanced electrocatalytic activity when it is exfoliated into single and few-layer sheets[35–38] or produced as nanoparticles.[39] The layered structure of $FePSe_3$ makes it also the material under consideration for cathodes in lithium batteries[30,40]

and for hydrogen storage.[41]

At ambient, low pressure (LP), $FePSe_3$ exists in the trigonal (space group no. 148, $R\bar{3}$) phase.[32] Its crystallographic structure (Fig. 1) is composed of 2D layers, which are parallel to the *ab*-plane and separated by the vdW gaps along the *c*-axis.[32] Each layer consists of Fe atoms octahedrally coordinated by six Se atoms and P atoms tetrahedrally coordinated by three Se atoms and one P atom, forming a $[P_2Se_6]^{4-}$ unit. The shortest distance between the adjacent Se layers (the vdW gap) is about 3.2 Å. There are two $FePSe_3$ formula units in the primitive unit cell but six formula units in the conventional unit cell with the atoms occupying the following Wyckoff positions: Fe 6c(0, 0, z), P 6c(0, 0, z) and Se 18f(x, y, z).

Upon application of pressure, $FePSe_3$ transforms into the monoclinic HP-I phase (space group no. 12, $C2/m$) with two $FePSe_3$ formula units in the primitive unit cell but four formula units in the conventional unit cell (Fig. 1). The transition pressure was predicted theoretically to be about 6 GPa.[34] The adjacent layers are separated by the narrower vdW gap of about 2.95 Å, besides, layer sliding occurs in the *ab*-plane placing the P–P atom pairs in the neighbouring layers on top of each other along the *c*-axis. The atoms occupy the following Wyckoff positions: Fe 4g(0, y, 0), P 4i(x, 0, z), Se1 4i(x, 0, z) and Se2 8j(x, y, z).

In the high-pressure (HP-II) phase (Fig. 1), observed experimentally above 8 GPa,[29] $FePSe_3$ crystal belongs to the space group no. 162, $P\bar{3}1m$, with the hexagonal lattice and two formula units in the primitive unit cell. The atoms occupy the following Wyckoff positions: Fe 2c(1/3, 2/3, 0), P 2e(0, 0, z) and Se 6k(x, 0, z). The transition to the HP-II phase is accompanied by abrupt spin-crossover transition and semiconductor-to-metal transition.[29] The latter is mainly determined by the in-plane metallization.[29] Note also that the resistivity of $FePSe_3$ changes stronger with pressure than with temperature.[29]

The mechanism of the pressure-driven SMT transition in $FePSe_3$ was studied[34] using first-principles calculations based on the plane-wave density functional theory (DFT) in the range from 0 to 35 GPa. The LP-to-HP-I phase transition was found to occur at about 6 GPa, whereas the second transition to the HP-II phase was predicted at 15 GPa.[34] The antiferromagnetic ordering was reproduced in the LP and HP-I phases in agreement with the experiment. The band gap of about 1.24 eV was found in the LP phase. It decreases to 0.72 eV at 10 GPa in the HP-I phase, and, finally, drops to zero in the metallic HP-II

phase.[34]

In our preceding study,[42] we considered the pressure-induced SMT in the crystalline iron thiophosphate ($FePS_3$) using first-principles DFT calculations, which confirmed the experimentally found SMT at about 15 GPa. Moreover, we found from the detailed analysis of the projected density of states that the 3p states of phosphorus atoms contribute significantly at the bottom of the conduction band, and the effect can be tuned by the relative displacement of phosphorus or sulfur atoms along the *c*-axis. Therefore, the collapse of the band gap occurs due to changes in the electronic structure of $FePS_3$ induced by relative displacements of phosphorus or sulfur atoms under pressure.

In the present study of SMT in $FePSe_3$, we made the same conclusion based not only on the change of the relative displacements of phosphorus or selenium atoms but also on the topological analysis of the pressure dependence of the P–P and Se–Se chemical bonds. The results of the topological analysis demonstrate that the new bonds appear between phosphorous atoms located in the neighbouring layers in the HP-II phase while they are absent in the other two phases (LP and HP-I).

2 METHODOLOGY

In the present study, the pressure-induced phase transitions in $FePSe_3$ have been investigated using the first-principle linear combination of atomic orbitals (LCAO) calculations using the CRYSTAL17 code.[43] The basis sets for Fe, P, and Se atoms have been chosen in the form of all-electron triple-zeta valence (TZV) basis sets augmented by one set of polarization functions (pob-TZVP).[44]

The evaluation of the Coulomb series and the exchange series has been done with the accuracy controlled by a set of tolerances, which were taken to be (10^{-8}, 10^{-8}, 10^{-8}, 10^{-8}, 10^{-16}). The integration in the Brillouin zone has been performed using the Monkhorst-Pack scheme[45] for an 8×8×8 **k**-point mesh. The SCF calculations were performed using Becke's 3-parameter functional (B3LYP-13%)[46] with a 10^{-10} tolerance on change in the total energy as in our previous study on $FePS_3$.[42] The percentage (13%) defines the Hartree-Fock admixture in the exchange part of DFT functional. All calculations were performed

using a restricted closed-shell hamiltonian, i.e., for non-magnetic structures. We believe that such approximation is consistent with the experimental temperature dependence of the electrical resistance (see Fig. 3 in Ref.[29]), which demonstrates the SMT in $FePSe_3$ in a wide range of temperatures up to 300 K, i.e., far above its Néel temperature of $T_N = 119$ K.[32]

The lattice parameters and atomic fractional coordinates were optimized for each selected pressure in the range of 0–30 GPa for three phases (Fig. 2): low-pressure (LP) trigonal (space group $R\bar{3}$) phase with rhombohedral lattice, high-pressure (HP-I) monoclinic (space group $C2/m$) phase, and high-pressure (HP-II) trigonal (space group $P\bar{3}1m$) phase with a hexagonal lattice. The starting structural parameters were taken from the experimental data for the LP $FePSe_3$ phase[32] and the related HP-I and HP-II $FePS_3$ phases.[47] The structure optimization at the required pressure was performed using the approach developed in Ref.[48]. The calculated lattice parameters (a, b, c, β), atomic fractional coordinates (x, y, z), the values of the band gap E_g and the atomic charges are reported in Table 1. The data for the $FePSe_3$ $R\bar{3}$ phase are reported in the hexagonal setting. The atomic charges were obtained using two methods – from the charge density distributions using the Bader procedure[1] and from the Mulliken population analysis.[49]

Calculated band structures and total/projected density of states (DOS) for the LP, HP-I and HP-II $FePSe_3$ phases are shown in Figs. 3 and 4, respectively. The high-symmetry points in the Brillouin zone for the three phases were selected following their definition on the Bilbao Crystallographic Server.[50] Note that in the rhombohedral space group $R\bar{3}$, belonging to the trigonal crystal system, two possible shapes of the Brillouin zone (and, respectively, sets of the high-symmetry points) are possible depending on the ratio between a and c lattice parameters.[50] In our case $\sqrt{3}a < \sqrt{2}c$ (Table 1) therefore the Brillouin zone has the topology of the truncated octahedron.

The phonon frequencies were computed at the center of the Brillouin zone (the Γ-point) within the harmonic approximation using the direct (frozen-phonon) method[43,51] for each $FePSe_3$ phase. The primitive cell of $FePSe_3$ in all phases includes 10 atoms (2 Fe, 2 P, and 6 Se), so that 30 phonon modes are expected and are classified as the three acoustic (A) modes with zero frequency, the Raman-active (R), infrared-active (IR) and silent (S) modes. The phonon frequencies calculated for three phases at P=0, 10, and 20 GPa are reported

in Table 2. Topological analysis of the electron density, according to the Quantum Theory of Atoms in Molecules,[1] was performed using the TOPOND code[52] in its parallel version,[53] which is incorporated in the CRYSTAL17 code.[43] Additionally, the calculations were also performed using the PBE0[54] and M06[55] functionals to check the sensitivity of the results of the topological analysis to the functional type.

Finally, we have performed the calculations of the electronic structure of $FePSe_3$ for several model structures with P atoms displaced along the c-axis. The crystal structures were fixed at the ones optimized for LP ($R\bar{3}$, 0 GPa), HP-I ($C2/m$, 10 GPa), and HP-II ($P\bar{3}1m$, 20 GPa) phases, while the displacement Δz(P) of the phosphorus atoms was varying between -0.1 Å and 0.6 Å. The obtained variations of the band gap E_g are shown in Fig. 5. Total and projected density of states (DOS) for the HP-I ($C2/m$, 10 GPa) $FePSe_3$ phase are shown for selected displacements Δz(P) in Fig. 6.

3 RESULTS AND DISCUSSION

3.1 Structural, Electronic and Phonon Properties

The calculated crystallographic parameters and band gap values for $FePSe_3$ in the LP (0 GPa), HP-I (10 GPa) and HP-II (20 GPa) phases are reported in Table 1. In the LP phase, the obtained results show rather good agreement with the available experimental lattice parameters[32] and band gap values,[56] however, the value of the c-axis parameter is overestimated.

The phonon frequencies were calculated to demonstrate the stability of three structures. The dimensions of the primitive unit cell do not change significantly across the LP(V=191 Å^3)-to-HP-I(V=193 Å^3) and HP-I(V=178 Å^3)-to-HP-II(V=173 Å^3) phase transitions, therefore the phonon instabilities are expected to occur at the Brillouin zone center[57]. The obtained phonon frequencies for the Raman and infrared active modes as well as silent modes are summarized in Table 2. The absence of any imaginary frequencies indicates that the optimized structures in all three phases of $FePSe_3$ correspond to a minimum on the surface of potential energy, making it possible to use the topological analysis (see below).

According to group-theoretical analysis for space group $R\bar{3}$ in the LP phase, the $5E_g$ and $5A_g$ even modes are Raman-active, whereas the $5E_u$ and $5A_u$ odd modes are infrared-active (two of them ($1E_u$ and $1A_u$) are acoustic modes with zero frequency at the Γ-point). The agreement between the theoretical and experimentally observed[58,59] phonon frequencies in the LP phase is good (Table 2). In the HP-I phase with the space group $C2/m$, the $7B_g$ and $8A_g$ even modes are Raman-active, whereas the $9B_u$ and $6A_u$ odd modes are infrared-active (three of them ($2B_u$ and $1A_u$) are acoustic modes with zero frequency at the Γ-point). In the HP-II phase with the space group $P\bar{3}1m$, the $5E_g$ and $3A_{1g}$ even modes are Raman-active, whereas the $5E_u$ and $4A_{2u}$ odd modes are infrared-active (two of them ($1E_u$ and $1A_{2u}$) are acoustic modes with zero frequency at the Γ-point). There are also three silent modes ($1A_{1u}$ and $2A_{2g}$) in HP-II phase. To the best of our knowledge, the experimental frequencies for the HP-I and HP-II phases are not available yet.

Pressure dependence of the band gap E_g in the LP, HP-I, and HP-II phases was evaluated from the band structure calculations (Fig. 3) performed for the optimized $FePSe_3$ crystal geometry (lattice parameters and atomic fractional coordinates) and is shown in the lower panel in Fig. 2. The band gap values were also estimated for respective space groups beyond the existence ranges of the HP-I and HP-II phases (shown by open circles in Fig. 2).

The transition from the low-pressure trigonal $R\bar{3}$ phase to the monoclinic HP-I $C2/m$ phase at 6 GPa is accompanied by a reduction of the volume and the number of layers in the conventional unit cell. Besides, in the HP-I phase the sliding of the adjacent layers occurs in the *ab*-plane leading to the positioning of the P–P atom pairs in the neighbouring layers on top of each other along the *c*-axis (Fig. 1). A variation in the band gap during the phase transition at 6 GPa does not show any abrupt jumps within the accuracy of our calculations.

The collapse of the band gap occurs in $FePSe_3$ during the SMT from the HP-I to HP-II phase at ∼13 GPa (Fig. 2). It is accompanied by a reduction of the unit cell volume by ∼3% and of the vdW gap d by ∼8%. Note that these numbers are about twice smaller than for $FePS_3$.[42] A simulated compression of the $FePSe_3$ lattice with the space group $C2/m$ under pressure up to 30 GPa as well as the simulated behaviour of the $FePSe_3$ lattice with the space group $P\bar{3}1m$ below 13 GPa do not result in any SMT (open circles in the lower panel in Fig. 2). It is important that in the HP-II phase phosphorous atoms are displaced

along the c-axis towards the vdW gap, so that they are located almost in the same plane together with selenium atoms. Similar behaviour under compression has been observed by us in $FePS_3$ where phosphorous atoms move to the sulfur plane.[42] Such displacement leads to an increase of the distance between two intralayer phosphorous atoms P_1 and P_2 and a decrease of the distance between two interlayer phosphorous atoms P_1 and P_3 (Fig. 1), thus modifying the interaction strength between them. This situation will be addressed in detail below using the topological analysis of the electron density.

The change of the electronic structure of $FePSe_3$ under pressure can be evidenced following its band structure (Fig. 3) and the projected density of states (DOS) (Fig. 4). The top of the valence bands in the LP and HP-I phases is mainly composed of the 3d(Fe) and 4p(Se) states, whereas the bottom of the conduction bands originates mainly from 3d(Fe), 3p(P) and 4p(Se) states. The contribution of the phosphorus atoms becomes particularly important in the HP-II phase, similarly to the case of $FePS_3$.[42]

Again, we found that the position of the phosphorus atoms, relative to the layer composed of the selenium atoms, is crucial for SMT. In Fig. 5, we present three structural models constructed using the optimized crystallographic structures for the LP (0 GPa), HP-I (10 GPa), and HP-II (20 GPa) phases. In these models, phosphorus atoms were displaced along the c-axis direction by Δz(P) (-0.1 Å $\leq \Delta z$(P)$\leq$ 0.6 Å) relative to their optimized positions. We found that the sufficiently large displacement of the phosphorus atoms in the direction of the plane formed by selenium atoms in the LP and HP-I phases (Fig. 1) leads to a decrease of the band gap and a transition to the metallic state. At the same time, the displacement of phosphorus atoms in the direction opposite to the plane formed by selenium atoms opens the gap in the HP-II phase for Δz(P)$>$ 0.3 Å.

The effect of the phosphorus atom displacements on the total and partial DOS is shown in Fig. 6 for the case of the HP-I phase at 10 GPa. As one can see, the electronic structure of $FePSe_3$ is determined by hybridization of the 3d(Fe), 3p(P), and 3p(S) states around the Fermi level. An increase of pressure leads to the relative displacement of the phosphorous atoms and promotes the broadening of both valence and conduction bands and a collapse of the band gap, i.e., insulator-to-metal transition. Thus, the SMT can be tuned by controlling the relative displacements of the phosphorous atoms.

3.2 Topological Analysis of P-P and Se-Se Chemical Bonds

The nature of chemical bonding in molecules and solids is defined by the electron density $\rho(\mathbf{r})$, conventionally considered to be weakly dependent on the calculation details such as, for example, the choice of the atomic basis and DFT functionals. This assumption is confirmed in the present work by comparing the results of the topological analysis based on the B3LYP-13%, PBE0 and M06 DFT calculations.

The topological analysis of the electron density of $FePSe_3$ was performed based on the Quantum Theory of Atoms in Molecules (QTAIM), due to Richard Bader and coworkers,[1] which is currently applied both to gas-phase molecules and solids. As a result of the analysis, a set of critical points (CPs), at which the density gradient vanishes ($\bigtriangledown\rho(\mathbf{r}) = 0$), was obtained and classified in terms of their type (r,s), where r is the rank, and s is the signature. Note that for stable three-dimensional structures, the critical points of $\rho(\mathbf{r})$ have rank 3 and correspond to the elements of the chemically recognizable structures in a crystal such as nuclei (3,-3), bonds (3,-1), rings (3,+1) and cages (3,+3).[52] The crystal electron density in each of the three $FePSe_3$ phases has the symmetry of a corresponding space group. Therefore, the sites ensured to be a CP can be nothing but those Wyckoff positions (WP)[60] of the corresponding space group.

While most of the QTAIM theory remains unaltered for solids, some significant differences should be taken into account.[61] The crystalline solid belongs to a three-dimensional torus.[61] As a consequence, the relationship, that connects the number of critical points (CP) of any molecular scalar field ($n-b+r-c = 1$), is replaced in the crystals by the Morse relationship[62] $n - b + r - c = 0$ for the crystal primitive unit cell. This relationship was used in the present work to check the total number of CPs in three phases of $FePSe_3$.

The CPs of electron density found in the topological analysis for $FePSe_3$ is related to WPs of the crystal space group, so that the WP multiplicity was used to determine the number of n, b, r and c type CPs.[4] The latter point is important since the search for CPs is realized by a procedure, depending on the search method and input parameters used in the TOPOND code.[52]

In Table 3 we report CPs and their WPs for three phases of $FePSe_3$ crystal. For example,

in the space group HP-II ($P\bar{3}1m$), Fe atoms (CP (3,-3)) occupy fixed WP 2c(1/3, 2/3, 0), whereas P and Se atoms (CPs (3,-3)) occupy 2e (one free-parameter) and 6k (two free-parameters) WPs with the local point symmetries C_{3v} and C_s, respectively. One can see from Table 3 that two CPs (3,-1) and (3,+3) appear at the WP 6k. Evidently, all CPs at the two-parameter WP 6k(x, 0, z) have different parameter values. Note that the obtained number of CPs fulfills the Morse relationship.[62]

The values of the electron density $\rho(\mathbf{r})$ and its Laplacian $\bigtriangledown^2\rho$ at the CP (3,-1) were used to evaluate the type of the interatomic bonds in $FePSe_3$. In particular, the positive (negative) value of the Laplacian means that the electron density at the point $\mathbf{r}$ is lower (higher) in value than it is on average in an infinitesimal volume around $\mathbf{r}$. Therefore, regions with positive Laplacian are locally charge depleted, while regions with negative Laplacian have locally concentrated charge. The location of CP (3,-1) on the interatomic line is a necessary condition for the existence of the chemical bond, whose classification into three groups (closed-shell (CS), shared-shell (SS) and intermediate-shell (IS)) was suggested in Refs.[63–66].

Table 4 shows the results of the topological analysis of the electron density and its Laplacian for selected P–P and Se–Se atom pairs in three $FePSe_3$ phases, corresponding to the different pressures. R_1 and R_2 are the distances from the CP (3,-1) to the bound atoms. It is seen that their sum R_1+R_2 is close to the value of the interatomic distance R for all (3,-1) CP's. This means that these CP's lie practically on the line connecting two atoms.

In Table 4, $P_1(Se_1)$–$P_2(Se_2)$ and $P_1(Se_1)$–$P_3(Se_3)$ are the intralayer and interlayer pairs of atoms, respectively. It is seen that at pressures just above the SMT (13 GPa and 20 GPa) the electron density at CP's of interlayer P_1–P_3 bonds is larger than that for intralayer P_1–P_2 bonds and both Se–Se interlayer bonds. Also, the Laplacian of the electron density for the P_1–P_3 interlayer bonds is negative, i.e., the electron charge is locally concentrated at the bond, whereas the Laplacian is positive for the P_1–P_2 intralayer and both Se–Se interlayer bonds. However, a further increase in pressure to 30 GPa leads to equalization of the electron density between the P_1–P_2 and P_1–P_3 bonds and the recovery of the P_1–P_2 intralayer bonds, as is evidenced by the negative Laplacian value. Thus, the results of the topological analysis demonstrate that the SMT is related to an increase of the electron density between P_1 and

P_3 atoms located in the different neighbouring layers, leading to the formation of the P_1–P_3 chemical bonds.

Besides the Laplacian, several other bond descriptors were evaluated for selected P–P and Se–Se bond CPs of $FePSe_3$ (Table 5). These are the potential energy density $V(\mathbf{r})$, the positive definite kinetic energy density $G(\mathbf{r})$ and the total electronic energy density $H(\mathbf{r}) = V(\mathbf{r}) + G(\mathbf{r})$.[4] Using these descriptors, the nature of bonds can be described.[4] Negative values of Laplacian and $H(\mathbf{r})$ and $|V(\mathbf{r})|/G(\mathbf{r}) > 2$ are attributed to the SS interactions such as covalent or polar bonds. Intermediate bonds are associated with IS interactions, which are described by positive Laplacian, an almost zero value of the total electronic energy density $H(\mathbf{r})$ and $1 < |V(\mathbf{r})|/G(\mathbf{r}) < 2$. Positive Laplacian and $H(\mathbf{r})$ and $|V(\mathbf{r})|/G(\mathbf{r}) < 1$ are indicative for the CS interactions such as ionic, hydrogen bonds and van der Waals interactions.

Detailed analysis of CPs for $P_1(Se_1)$–$P_2(Se_2)$ and $P_1(Se_1)$–$P_3(Se_3)$ bonds at three pressures $P = 0$, 10, and 20 GPa is given in Table 5. One can classify $P_1(Se_1)$–$P_2(Se_2)$ and $P_1(Se_1)$–$P_3(Se_3)$ bonds over CS, SS and IS types at three selected pressures. According to the classification scheme, described above, the intralayer P_1–P_2 bonds can be described as the shared-shell covalent bonds in the LP and HP-I phases (at the pressures 0 GPa and 10 GPa, respectively) with negative $\bigtriangledown^2\rho(\mathbf{r})$, $|V(\mathbf{r})|/G(\mathbf{r}) > 2$, negative total energy density $H(\rho(\mathbf{r}))$ and the kinetic energy per electron $G(\mathbf{r})/\rho(\mathbf{r}) < 1$. In the HP-II phase (at 20 GPa), the P_1–P_2 bond type change to the intermediate shell bond with positive $\bigtriangledown^2\rho(\mathbf{r})$ and $1 < |V(\mathbf{r})|/G(\mathbf{r}) < 2$. The total energy density $H(\rho(\mathbf{r}))$ remains negative (but becomes about five times smaller), while $G(\mathbf{r})/\rho(\mathbf{r})$ remains mostly the same. Note that the interlayer P_1–P_3 bonds are absent in the LP and HP-I phases but appear in the HP-II phase and can be classified as the shared-shell covalent bonds ($\bigtriangledown^2\rho(\mathbf{r}) < 0$, $|V(\mathbf{r})|/G(\mathbf{r}) > 2$, $H(\rho(\mathbf{r})) < 0$ and $G(\mathbf{r})/\rho(\mathbf{r}) < 1$), which are weaker than the P_1–P_2 SS bonds for two lower pressures. The interlayer Se_1–Se_2 and Se_1–Se_3 bonds also change with increasing pressure and can be classified as the intermediate shell bonds: $\bigtriangledown^2\rho(\mathbf{r})$ is always small, but remains positive; $|V(\mathbf{r})|/G(\mathbf{r})$ grows from 0.7 to 1.1 with increasing pressure, the total energy density $H(\rho(\mathbf{r}))$ is very small positive in the LP and HP-I phases at the two smaller pressures and becomes negative in the HP-II phase at 20 GPa; $G(\mathbf{r})/\rho(\mathbf{r})$ is less than 1 but larger than for the P–P

bonds.

The results of the topological analysis for the PBE0 and M06 functionals are shown in Table 6. They are qualitatively similar to those obtained using the B3LYP-13% functional thus allowing to withdraw the same conclusions regarding the chemical bonding in $FePSe_3$.

The electron localization function (ELF) contour maps for LP (0 GPa), HP-I (10 GPa), and HP-II (20 GPa) phases of $FePSe_3$ are shown in Fig. 7 for selected planes, being orthogonal to the vdW gaps and containing P–P atom pairs. The vdW gaps with low electron density are well observed in the LP phase between layers. The P–P atom pairs located in the neighbouring layers are displaced along the *b*-axis that makes P_1 and P_3 phosphorus atoms well separated (Fig. 1). Upon phase transition to the HP-I phase, the adjacent layers displace relative to each other and come closer, however, they are still separated by the vdW gaps, visible in Fig. 7. While the P–P atom pairs located in the neighbouring layers are situated on top of each other along the *c*-axis, they are now displaced along the *a*-axis (therefore P_3 atom is not visible in the HP-I phase in Fig. 7), thus preventing the bonding between the P_1 and P_3 phosphorus atoms (see also Fig. 1). Finally, upon SMT at 13 GPa, the van der Waals gaps vanish, and P_1 and P_3 phosphorus atoms, located in LP and HP-I phases in different layers, become strongly bound along the *c*-axis. This fact is well observed in the ELF contour map of the HP-II phase as an increase of the electron localization in the interatomic region between the two phosphorus P_1 and P_3 located in different layers, which is accompanied by a slight reduction of electron localization between P_1 and P_2 atoms located in the same layer.

4 CONCLUSIONS

The behaviour of the structural, electronic and phonon properties in the layered iron phosphorus triselenide ($FePSe_3$) under pressure has been theoretically studied based on the first-principles LCAO calculations using hybrid DFT-HF B3LYP functional. Detailed analysis of the chemical bonding in $FePSe_3$ has been performed using the topological analysis of the electron density, according to the Quantum Theory of Atoms in Molecules.[1]

Two pressure-induced phase transitions have been evidenced at about 6 GPa and 13 GPa, in agreement with the recent experimental[29] and theoretical[34] findings. At ambient

pressure, $FePSe_3$ has the indirect band gap of about 1.6 eV, compared to the experimental value of 1.3 eV.[30] The first phase transition is accompanied by a change in symmetry from $R\bar{3}$ to $C2/m$, sliding of adjacent layers in the ab-plane and a small reduction of the band gap down to about 1.2-1.4 eV. At the second phase transition from $C2/m$ to $P\bar{3}1m$ phase, the band gap collapses, and $FePSe_3$ transforms to the metallic state. Moreover, similar to the case of $FePS_3$,[42] metallic conductivity in $FePSe_3$ could also occur in the LP and HP-I phases if the P and Se atoms were located almost in the same plane.

The analysis of the projected density of states suggests that the 3p states of phosphorus atoms contribute significantly to the bottom of the conduction band. Therefore, the collapse of the band gap upon the SMT at about 13 GPa is caused by changes in the electronic structure of $FePSe_3$ induced by relative displacements of phosphorus or selenium atoms along the c-axis direction under pressure. The topological analysis of the electron density and its Laplacian in $FePSe_3$ suggests that the pressure affects not only interatomic distances but the bond nature between the intralayer and interlayer phosphorus atoms. In particular, the type of the intralayer P–P bonds changes from the shared-shell covalent bonds in the LP and HP-I phases to the intermediate-shell bond in the HP-II phase. At the same time, the interlayer P–P bonds, absent in the LP and HP-I phases, appear in the HP-II phase as the shared-shell covalent bonds.

ACKNOWLEDGMENTS

The authors acknowledge the assistance of the University Computer Center of Saint-Petersburg State University in the accomplishment of high-performance computations. A.K. is grateful to the Latvian Council of Science project no. lzp-2018/2-0353 for financial support. Institute of Solid State Physics, University of Latvia as the Center of Excellence has received funding from the European Union's Horizon 2020 Framework Programme H2020-WIDESPREAD-01-2016-2017-TeamingPhase2 under grant agreement No. 739508, project CAMART2.

References

1. R. F. W. Bader, *Atoms in Molecules: A Quantum Theory* (Clarendon Press, Oxford, 1994).

2. C. Lepetit, P. Fau, K. Fajerwerg, M. L. Kahn, and B. Silvi, Coord. Chem. Rev. **345**, 150 (2017).

3. S. F. Vyboishchikov, A. Sierraalta, and G. Frenking, J. Comput. Chem. **18**, 416 (1997).

4. C. Gatti, Z. Kristallogr. **220**, 399 (2005).

5. E. R. Johnson, S. Keinan, P. Mori-Sánchez, J. Contreras-García, A. J. Cohen, and W. Yang, J. Am. Chem. Soc. **132**, 6498 (2010).

6. C. F. Matta and A. A. Arabi, Future Med. Chem. **3**, 969 (2011).

7. A. Krawczuk and P. Macchi, Chem. Cent. J. **8**, 68 (2014).

8. N. L. Marana, S. Casassa, E. Longo, and J. R. Sambrano, J. Phys. Chem. C **120**, 6814 (2016).

9. B. Dittrich, Acta Crystallogr. B **73**, 325 (2017).

10. P. Macchi, Acta Crystallogr. B **73**, 330 (2017).

11. P. R. Varadwaj, A. Varadwaj, H. M. Marques, and K. Yamashita, Sci. Rep. **9**, 50 (2019).

12. J. T. Titah, F. C. Ngwa, P. Sirsch, C. W. Karime, and M. G. R. Kone, Int. J. Comput. Theor. Chem. **7**, 115 (2019).

13. L. H. S. Lacerda, R. A. P. Ribeiro, and S. R. de Lazaro, J. Magn. Magn. Mater. **480**, 199 (2019).

14. D. Korabel'nikov and Y. N. Zhuravlev, RSC Adv. **9**, 12020 (2019).

15. K. Tolborg and B. B. Iversen, Chem. Eur. J. **25**, 15010 (2019).

16. F. Parisi, L. Sciascia, F. Princivalle, and M. Merli, Phys. Chem. Minerals **39**, 103 (2012).

17. M. Merli and L. Sciascia, Phys. Chem. Minerals **40**, 455 (2013).

18. M. A. Salvadó, P. Pertierra, A. Morales-García, J. M. Menéndez, and J. M. Recio, J. Phys. Chem. C **117**, 8950 (2013).

19. N. Casati, A. Kleppe, A. P. Jephcoat, and P. Macchi, Nat. Commun. **7**, 10901 (2016).

20. A. L. J. Pereira, O. Gomis, J. A. Sans, J. Contreras-García, F. J. Manjón, P. Rodríguez-Hernández, A. Muñoz, and A. Beltrán, Phys. Rev. B **93**, 224111 (2016).

21. M. Merli and A. Pavese, Acta Crystallogr. A **74**, 102 (2018).

22. S. Belarouci, T. Ouahrani, N. Benabdallah, A. Morales-García, and R. Franco, Phase Transit. **91**, 759 (2018).

23. U. Schwarz, A. Wosylus, M. Schmidt, L. Akselrud, A. Ormeci, M. Hanfland, V. Hermann, and C. Kuntscher, Inorganics **7**, 143 (2019).

24. B. Meyer, S. Barthel, A. Mace, L. Vannay, B. Guillot, B. Smit, and C. Corminboeuf, J. Phys. Chem. Lett. **10**, 1482 (2019).

25. F. Parisi, L. Sciascia, F. Princivalle, and M. Merli, Ceram. Int. **45**, 2820 (2019).

26. R. Gajda, M. Stachowicz, A. Makal, S. Sutuła, J. Parafiniuk, P. Fertey, and K. Woźniak, IUCrJ **7**, 383 (2020).

27. H. Kasai, K. Tolborg, M. Sist, J. Zhang, V. R. Hathwar, M. O. Filsø, S. Cenedese, K. Sugimoto, J. Overgaard, E. Nishibori, et al., Nat. Mater. **17**, 249 (2018).

28. M. R. Ryzhikov, V. A. Slepkov, S. G. Kozlova, and S. P. Gabuda, J. Comput. Chem. **35**, 1641 (2014).

29. Y. Wang, J. Ying, Z. Zhou, J. Sun, T. Wen, Y. Zhou, N. Li, Q. Zhang, F. Han, Y. Xiao, et al., Nat. Commun. **9**, 1914 (2018).

30. R. Brec, D. M. Schleich, G. Ouvrard, A. Louisy, and J. Rouxel, Inorg. Chem. **18**, 1814 (1979).

31. B. Taylor, J. Steger, A. Wold, and E. Kostiner, Inorg. Chem. **13**, 2719 (1974).

32. A. Wiedenmann, J. Rossat-Mignod, A. Louisy, R. Brec, and J. Rouxel, Solid State Commun. **40**, 1067 (1981).

33. G. Le Flem, R. Brec, G. Ouvard, A. Louisy, and P. Segransan, J. Phys. Chem. Solids **43**, 455 (1982).

34. Y. Zheng, X.-X. Jiang, X.-X. Xue, J. Dai, and Y. Feng, Phys. Rev. B **100**, 174102 (2019).

35. R. Gusmão, Z. Sofer, D. Sedmidubský, Š. Huber, and M. Pumera, ACS Catalysis **7**, 8159 (2017).

36. D. Mukherjee, P. M. Austeria, and S. Sampath, ACS Appl. Energy Mater. **1**, 220 (2018).

37. M. Barua, M. M. Ayyub, P. Vishnoi, K. Pramoda, and C. N. R. Rao, J. Mater. Chem. A **7**, 22500 (2019).

38. Y. Hao, A. Huang, S. Han, H. Huang, J. Song, X. Sun, Z. Wang, L. Li, F. Hu, J. Xue, et al., ACS Appl. Mater. Interfaces **12**, 29393 (2020).

39. J. Yu, W.-J. Li, H. Zhang, F. Zhou, R. Li, C.-Y. Xu, L. Zhou, H. Zhong, and J. Wang, Nano Energy **57**, 222 (2019).

40. R. Brec, Solid State Ionics **22**, 3 (1986).

41. N. Ismail, A. El-Meligi, Y. Temerk, and M. Madian, Int. J. Hydrog. Energy **35**, 7827 (2010).

42. R. A. Evarestov and A. Kuzmin, J. Comput. Chem. **41**, 1337 (2020).

43. R. Dovesi, A. Erba, R. Orlando, C. M. Zicovich-Wilson, B. Civalleri, L. Maschio, M. Rérat, S. Casassa, J. Baima, S. Salustro, et al., WIREs Comput. Mol. Sci. **8**, e1360 (2018).

44. D. V. Oliveira, J. Laun, M. F. Peintinger, and T. Bredow, J. Comput. Chem. **40**, 2364 (2019).

45. H. J. Monkhorst and J. D. Pack, Phys. Rev. B **13**, 5188 (1976).

46. A. D. Becke, J. Chem. Phys. **98**, 5648 (1993).

47. C. R. S. Haines, M. J. Coak, A. R. Wildes, G. I. Lampronti, C. Liu, P. Nahai-Williamson, H. Hamidov, D. Daisenberger, and S. S. Saxena, Phys. Rev. Lett. **121**, 266801 (2018).

48. A. J. Jackson, J. M. Skelton, C. H. Hendon, K. T. Butler, and A. Walsh, J. Chem. Phys. **143**, 184101 (2015).

49. R. S. Mulliken, J. Chem. Phys. **23**, 1833 (1955).

50. M. I. Aroyo, D. Orobengoa, G. de la Flor, E. S. Tasci, J. M. Perez-Mato, and H. Wondratschek, Acta Crystallogr. A **70**, 126 (2014).

51. F. Pascale, C. M. Zicovich-Wilson, F. López Gejo, B. Civalleri, R. Orlando, and R. Dovesi, J. Comput. Chem. **25**, 888 (2004).

52. C. Gatti, V. R. Saunders, and C. Roetti, J. Chem. Phys. **101**, 10686 (1994).

53. S. Casassa, A. Erba, J. Baima, and R. Orlando, J. Comput. Chem. **36**, 1940 (2015).

54. C. Adamo and V. Barone, J. Chem. Phys. **110**, 6158 (1999).

55. Y. Zhao and D. G. Truhlar, Theor. Chem. Account. **120**, 215 (2008).

56. K.-Z. Du, X.-Z. Wang, Y. Liu, P. Hu, M. I. B. Utama, C. K. Gan, Q. Xiong, and C. Kloc, ACS Nano **10**, 1738 (2016).

57. S. Baroni, S. de Gironcoli, A. Dal Corso, and P. Giannozzi, Rev. Mod. Phys. **73**, 515 (2001).

58. M. Scagliotti, M. Jouanne, M. Balkanski, G. Ouvrard, and G. Benedek, Phys. Rev. B **35**, 7097 (1987).

59. M. Bernasconi, G. L. Marra, G. Benedek, L. Miglio, M. Jouanne, C. Julien, M. Scagliotti, and M. Balkanski, Phys. Rev. B **38**, 12089 (1988).

60. E. Kroumova, M. Aroyo, J. Perez-Mato, A. Kirov, C. Capillas, S. Ivantchev, and H. Wondratschek, Phase Transit. **76**, 155 (2003).

61. V. Luaña, M. A. Blanco, A. Costales, P. Mari-Sánchez, and A. M. Pendás, in *The Quantum Theory of Atoms in Molecules: From Solid State to DNA and Drug Design*, edited by C. F. Matta and R. J. Boyd (Wiley-VCH Verlag GmBH, Darmstadt, 2007), chap. 8, pp. 207–229.

62. M. Morse and S. S. Cairns, *Critical Point Theory in Global Analysis and Differential Geometry* (Academic Press, New York, 1969).

63. D. Cremer and E. Kraka, Croat. Chem. Acta. **57**, 1259 (1984).

64. E. Espinosa, I. Alkorta, J. Elguero, and E. Molins, J. Chem. Phys. **117**, 5529 (2002).

65. D. Marabello, R. Bianchi, G. Gervasio, and F. Cargnoni, Acta Crystallogr. A **60**, 494 (2004).

66. V. G. Tsirelson, *Quantum Chemistry. Molecules Molecular Systems and Solids* (Binom Publ., Moscow, 2014).

67. K. Momma and F. Izumi, J. Appl. Crystallogr. **44**, 1272 (2011).

Figure 1: Crystallographic structure of $FePSe_3$ in the low-pressure (LP, P=0 GPa) trigonal (space group $R\bar{3}$) phase, intermediate pressure (HP-I, P=10 GPa) monoclinic (space group $C2/m$) phase and high-pressure (HP-II, P=20 GPa) trigonal (space group $P\bar{3}1m$) phase. Conventional unit cells are shown. The distance between the two adjacent layers is denoted as d. The illustrations were created using the VESTA software.[67]

Figure 2: Pressure dependence of the calculated lattice parameters and the band gap E_g in $FePSe_3$. Open circles in the lower panel show extrapolation of the band gap beyond the HP-I and HP-II phase existence ranges.

Figure 3: Band structure diagram for the LP, HP-I, and HP-II $FePSe_3$ phases. The energy zero is set at the top of the valence band (Fermi energy position).

Figure 4: Total and projected density of states (DOS) for the LP, HP-I, and HP-II $FePSe_3$ phases. The energy zero is set at the top of the valence band (Fermi energy position).

Figure 5: Dependence of the band gap E_g in LP, HP-I, and HP-II $FePSe_3$ phases on the displacement of phosphorus atoms Δz(P) along the c-axis.

Figure 6: Total and projected density of states (DOS) for the HP-I ($C2/m$) $FePSe_3$ phase as a function of phosphorus atoms displacement Δz(P) along the c-axis. The energy zero is set at the top of the valence band (Fermi energy position).

Figure 7: The electron localization function (ELF) contour maps for LP (0 GPa), HP-I (10 GPa), and HP-II (20 GPa) phases of $FePSe_3$. Selected atoms are indicated. Atom numbering is as in Fig. 1.

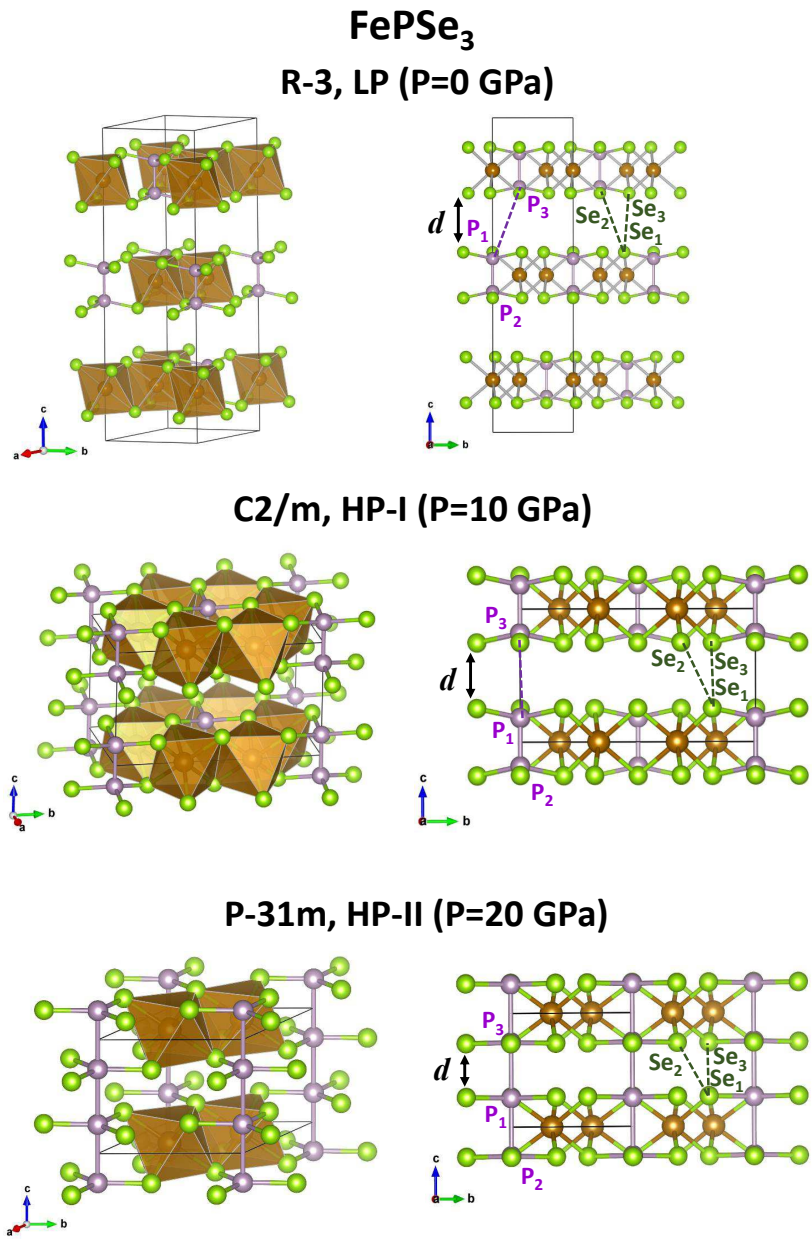

Figure 1
R. A. Evarestov, A. Kuzmin
J. Comput. Chem.

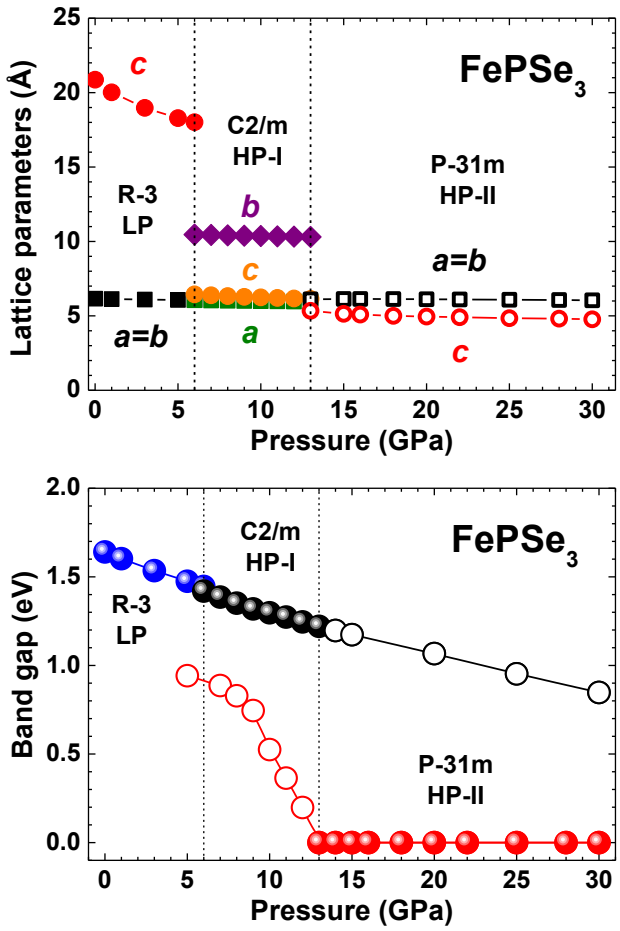

Figure 2
R. A. Evarestov, A. Kuzmin
J. Comput. Chem.

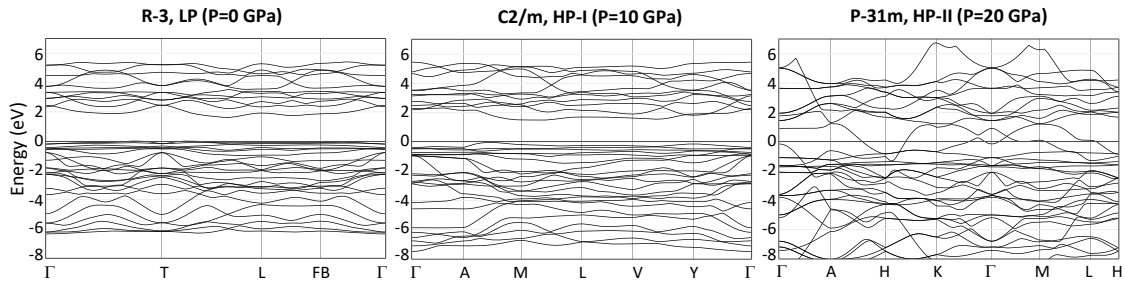

Figure 3
R. A. Evarestov, A. Kuzmin
J. Comput. Chem.

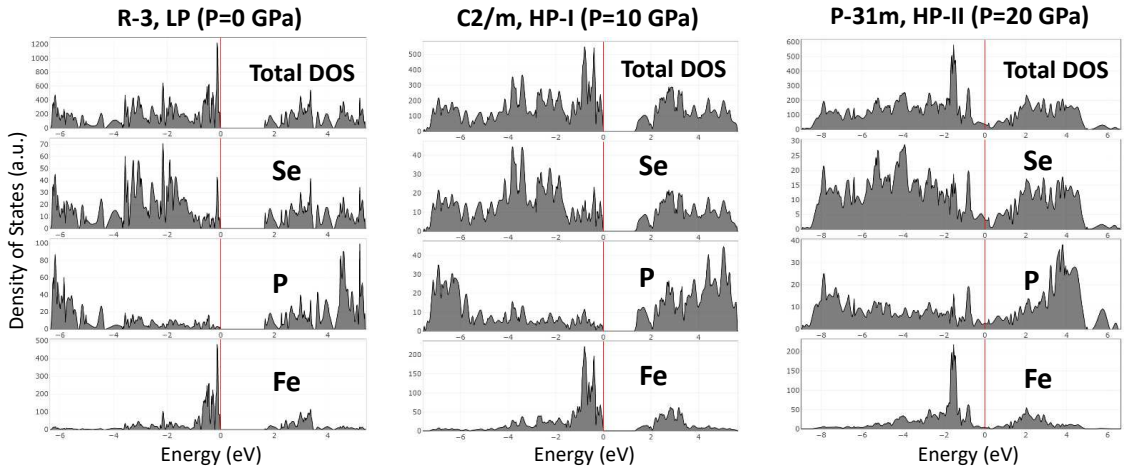

Figure 4
R. A. Evarestov, A. Kuzmin
J. Comput. Chem.

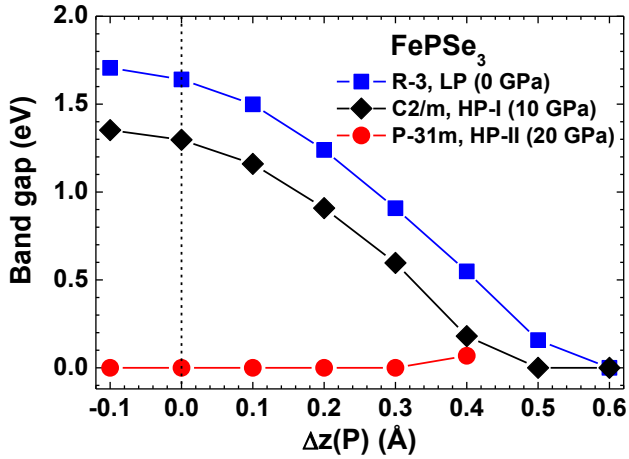

Figure 5
R. A. Evarestov, A. Kuzmin
J. Comput. Chem.

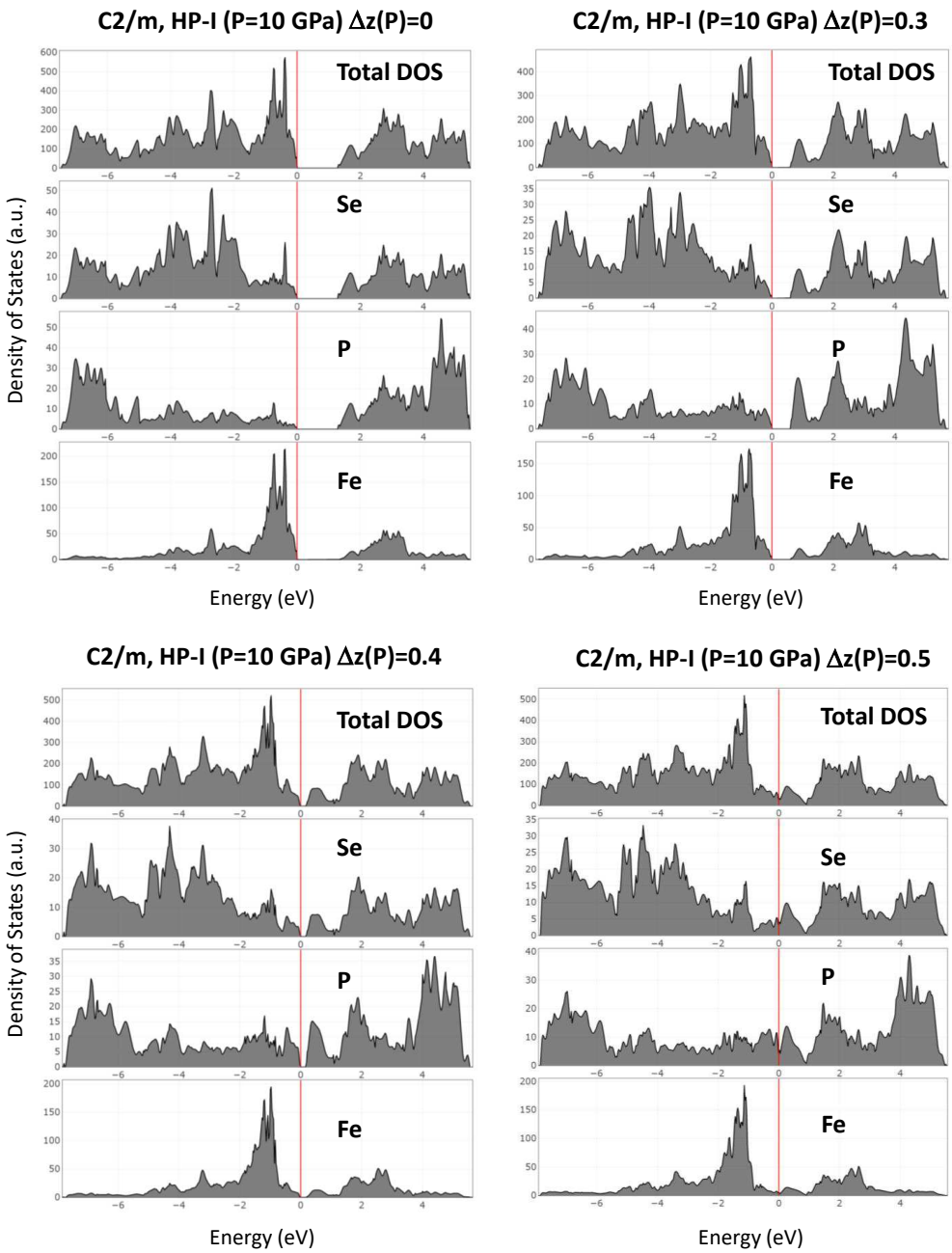

Figure 6
R. A. Evarestov, A. Kuzmin
J. Comput. Chem.

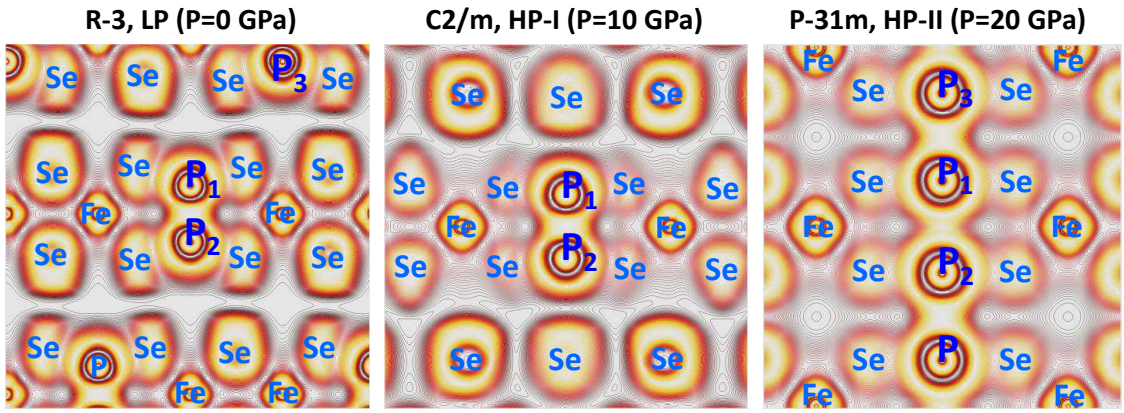

Figure 7
R. A. Evarestov, A. Kuzmin
J. Comput. Chem.

Table 1: Crystallographic parameters, band gap values and atomic charges for $FePSe_3$ at 0, 10, and 20 GPa. Experimental data are taken from Refs.[32,56].

	Space group $R\bar{3}$ (148) LP (P=0 GPa)		Space group $C2/m$ (12) HP-I (P=10 GPa)	Space group $P\bar{3}1m$ (162) HP-II (P=20 GPa)
	Experiment[32]	LCAO	LCAO	LCAO
a (Å)	6.262	6.154	5.989	6.118
b (Å)			10.37	
c (Å)	19.81	20.87	6.244	4.953
β (°)			108.8	
y(Fe)			0.3333	
z(Fe)	0.1667	0.1665		
x(P)			0.0628	
z(P)	0.4486	0.4477	0.1824	-0.2565
x(Se1)	0.3282	0.3340	-0.2836	0.3700
y(Se1)	0.0073	0.0320		
z(Se1)	0.0801	0.0925	0.2513	-0.2637
x(Se2)			0.2686	
y(Se2)			0.1849	
z(Se2)			0.2492	
E_g (eV)	1.3[56]	1.6	1.3	0
			Bader charges	
Fe		0.52	0.40	0.26
P		0.19	0.19	0.12
Se1		-0.23	-0.22	-0.13
Se2			-0.18	
			Mulliken charges	
Fe		0.29	0.16	-0.13
P		0.60	0.62	0.47
Se1		-0.30	-0.30	-0.11
Se2			-0.24	

Table 2: Calculated phonon frequencies (in cm^{-1}) at the Γ-point for $FePSe_3$ at P=0, 10, and 20 GPa. Acoustic (A), Raman active (R), infrared active (IR), and silent (S) modes are indicated. The experimental infrared and Raman frequencies (exp.) measured at room temperature[58,59] are also reported for comparison.

Space group $R\bar{3}$ (148) LP (P=0 GPa)				Space group $C2/m$ (12) HP-I (P=10 GPa)			Space group $P\bar{3}1m$ (162) HP-II (P=20 GPa)		
Mode	Frequency	Frequency (exp.)	Activity	Mode	Frequency	Activity	Mode	Frequency	Activity
E_u	0		A	A_u	0	A	A_{2u}	0	A
A_u	0		A	B_u	0	A	E_u	0	A
A_g	111	74	R	B_u	0	IR	A_{2u}	122	IR
A_u	118	108	IR	B_u	110	IR	A_{2g}	150	S
E_g	122	117	R	B_g	121	R	E_u	160	IR
E_u	131	126	IR	B_g	140	R	E_g	174	R
E_g	154	139	R	A_g	141	R	A_{1g}	180	R
A_g	158	150	R	B_u	158	IR	E_g	194	R
E_u	160	159	IR	A_u	161	IR	E_u	195	IR
A_u	165		IR	B_u	167	IR	A_{2u}	197	IR
E_g	178	172	R	B_g	172	R	E_g	212	R
A_g	202	218	R	A_g	172	R	A_{1u}	238	S
A_u	212		IR	A_u	177	IR	A_{1g}	243	R
A_g	230		R	A_g	193	R	A_{1g}	263	R
E_u	257		IR	B_g	195	R	A_{2u}	320	IR
E_g	267		R	A_u	201	IR	A_{2g}	321	S
A_u	288	305	IR	A_g	202	R	E_u	331	IR
E_u	393	442	IR	A_g	227	R	E_g	333	R
E_g	395	450	R	B_u	243	IR	E_g	414	R
A_g	516	506	R	B_g	279	R	E_u	432	IR
				Au	295	IR			
				Bu	295	IR			
				Bu	301	IR			
				Ag	308	R			
				Bg	309	R			
				Ag	428	R			
				Bu	430	IR			
				Bg	430	R			
				Au	434	IR			
				Ag	530	R			

Table 3: Critical points and their Wyckoff positions (WP) in the primitive cell of $FePSe_3$. The Morse relationships $n-b+r-c=0$ as expected in crystalline materials ($30-87+99-42=0$ for LP, $10-25+28-13=0$ for HP-I and $10-29+27-8=0$ for HP-II).

LP ($R\bar{3}$)				HP-I ($C2/m$)				HP-II ($P\bar{3}1m$)			
CP No.	CP type		WP	CP No.	CP type		WP	CP No.	CP type		WP
1	(3,-3)	n	6c (Fe)	1	(3,-3)	n	2g (Fe)	1	(3,-3)	n	2c (Fe)
2	(3,-3)	n	6c (P)	2	(3,-3)	n	2i (P)	2	(3,-3)	n	2e (P)
3	(3,-3)	n	18f (Se)	3	(3,-3)	n	2i (Se1)	3	(3,-3)	n	6k (Se)
4	(3,-1)	b	18f	4	(3,-3)	n	4j (Se2)	4	(3,-1)	b	6k
5	(3,-1)	b	18f	5	(3,-1)	b	4j	5	(3,-1)	b	12l
6	(3,-1)	b	9e	6	(3,-1)	b	4j	6	(3,-1)	b	6j
7	(3,-1)	b	6c	7	(3,-1)	b	4j	7	(3,-1)	b	3g
8	(3,-1)	b	18f	8	(3,-1)	b	1a	8	(3,-1)	b	1a
9	(3,-1)	b	18f	9	(3,-1)	b	4j	9	(3,-1)	b	1b
10	(3,+1)	r	9d	10	(3,-1)	b	2i	10	(3,+1)	r	3f
11	(3,+1)	r	18f	11	(3,-1)	b	2i	11	(3,+1)	r	12l
12	(3,+1)	r	18f	12	(3,-1)	b	2f	12	(3,+1)	r	6i
13	(3,+1)	r	18f	13	(3,-1)	b	2h	13	(3,+1)	r	6j
14	(3,+1)	r	18f	14	(3,+1)	r	4j	14	(3,+3)	c	6k
15	(3,+1)	r	18f	15	(3,+1)	r	1d	15	(3,+3)	c	2d
16	(3,+3)	c	6c	16	(3,+1)	r	1c				
17	(3,+3)	c	18f	17	(3,+1)	r	1b				
18	(3,+3)	c	18f	18	(3,+1)	r	4j				
				19	(3,+1)	r	4j				
				20	(3,+1)	r	2i				
				21	(3,+1)	r	4j				
				22	(3,+1)	r	4j				
				23	(3,+1)	r	2g				
				24	(3,+3)	c	2e				
				25	(3,+3)	c	2h				
				26	(3,+3)	c	4j				
				27	(3,+3)	c	2i				
				28	(3,+3)	c	4j				

Table 4: Results of the topological analysis of the electron density (ρ) and its Laplacian ($\bigtriangledown^2\rho$) for selected P–P and Se–Se atom pairs (see Fig. 1) in three phases (LP ($R\bar{3}$), HP-I ($C2/m$) and HP-II ($P\bar{3}1m$)) of $FePSe_3$ at several pressures calculated using the B3LYP-13% functional. R is the interatomic distance, $R_1 + R_2$ is the sum of distances from the critical point to the atoms. See text for details.

P (GPa)	Atom pair	R (Å)	ρ (a.u.)	$\bigtriangledown^2\rho$ (a.u.)	$R_1 + R_2$ (Å)	CP type
			LP ($R\bar{3}$)			
0	P_1–P_2	2.182	0.129	-0.219	2.182	(3,-1)
	P_1–P_3	5.952				no bond
	Se_1–Se_2	4.390	0.003	0.007	4.396	(3,-1)
	Se_1–Se_3	4.532	0.002	0.007	4.535	(3,-1)
3	P_1–P_2	2.173	0.131	-0.227	2.173	(3,-1)
	P_1–P_3	5.444				no bond
6	P_1–P_2	2.163	0.134	-0.237	2.162	(3,-1)
	P_1–P_3	5.196				no bond
			HP-I ($C2/m$)			
6	P_1–P_2	2.165	0.134	-0.238	2.165	(3,-1)
	P_1–P_3	4.456				no bond
10	P_1–P_2	2.157	0.136	-0.248	2.157	(3,-1)
	P_1–P_3	4.268				no bond
	Se_1–Se_2	3.483	0.013	0.028	3.485	(3,-1)
	Se_1–Se_3	3.450	0.014	0.029	3.453	(3,-1)
13	P_1–P_2	2.152	0.137	-0.254	2.152	(3,-1)
	P_1–P_3	4.171				no bond
			HP-II ($P\bar{3}1m$)			
13	P_1–P_2	3.047	0.022	0.040	3.047	(3,-1)
	P_1–P_3	2.293	0.109	-0.136	2.293	(3,-1)
20	P_1–P_2	2.541	0.063	0.010	2.541	(3,-1)
	P_1–P_3	2.413	0.089	-0.061	2.413	(3,-1)
	Se_1–Se_2	2.830	0.039	0.074	2.836	(3,-1)
	Se_1–Se_3	3.256	0.020	0.042	3.260	(3,-1)
30	P_1–P_2	2.369	0.087	-0.045	2.369	(3,-1)
	P_1–P_3	2.402	0.090	-0.062	2.402	(3,-1)

Table 5: Several properties (the electron density ρ and its Laplacian $\bigtriangledown^2\rho$, the $|V(\mathbf{r})|/G(\mathbf{r})$ ratio, the total energy density $H(\mathbf{r})$ (all in atomic units) and the kinetic energy per electron $G(\mathbf{r})/\rho(\mathbf{r})$) calculated for the selected P–P and Se–Se (see Fig. 1) bond CPs of $FePSe_3$ at three pressures P (in GPa) using the B3LYP-13% functional. R (in Å) is the interatomic distance. See text for details.

P	Atom pair	R	ρ	$\bigtriangledown^2\rho$	$\lvert V(\mathbf{r})\rvert/G(\mathbf{r})$	$H(\mathbf{r})$	$G(\mathbf{r})/\rho(\mathbf{r})$	CP type
				LP ($R\bar{3}$)				
0	P_1–P_2	2.182	0.129	-0.219	4.226	-0.079	0.190	(3,-1)
	P_1–P_3	5.952						no bond
	Se_1–Se_2	4.390	0.003	0.007	0.778	0.000	0.495	(3,-1)
	Se_1–Se_3	4.532	0.002	0.007	0.723	0.000	0.535	(3,-1)
				HP-I ($C2/m$)				
10	P_1–P_2	2.157	0.136	-0.248	4.381	-0.088	0.191	(3,-1)
	P_1–P_3	4.268						no bond
	Se_1–Se_2	3.483	0.013	0.028	0.964	0.000	0.500	(3,-1)
	Se_1–Se_3	3.450	0.014	0.029	0.961	0.000	0.500	(3,-1)
				HP-II ($P\bar{3}1m$)				
20	P_1–P_2	2.541	0.063	0.010	1.867	-0.017	0.223	(3,-1)
	P_1–P_3	2.413	0.089	-0.061	2.774	-0.035	0.308	(3,-1)
	Se_1–Se_2	2.830	0.039	0.074	1.115	-0.002	0.529	(3,-1)
	Se_1–Se_3	3.256	0.020	0.042	1.058	-0.001	0.548	(3,-1)

Table 6: The results of topological analysis (as in Table 5) for the PBE0 and M06 DFT functionals illustrating weak sensitivity of properties to the functional type.

P	Atom pair	R	ρ	$\bigtriangledown^2\rho$	$\lvert V(\mathbf{r})\rvert/G(\mathbf{r})$	$H(\mathbf{r})$	$G(\mathbf{r})/\rho(\mathbf{r})$	CP type
				LP ($R\bar{3}$) PBE0				
0	P_1–P_2	2.150	0.137	-0.260	4.584	-0.090	0.183	(3,-1)
	P_1–P_3	5.711						no bond
	Se_1–Se_2	4.127	0.005	0.010	0.876	0.000	0.468	(3,-1)
	Se_1–Se_3	4.261	0.004	0.009	0.842	0.000	0.490	(3,-1)
				LP ($R\bar{3}$) M06				
0	P_1–P_2	2.157	0.134	-0.240	4.333	-0.086	0.192	(3,-1)
	P_1–P_3	5.579						no bond
	Se_1–Se_2	3.985	0.006	0.012	0.926	0.000	0.466	(3,-1)
	Se_1–Se_3	4.130	0.005	0.011	0.897	0.000	0.483	(3,-1)
				HP-I ($C2/m$) PBE0				
10	P_1–P_2	2.130	0.143	-0.286	4.704	-0.098	0.185	(3,-1)
	P_1–P_3	4.210						no bond
	Se_1–Se_2	3.382	0.016	0.033	0.975	0.000	0.512	(3,-1)
	Se_1–Se_3	3.405	0.015	0.032	0.976	0.000	0.513	(3,-1)
				HP-I ($C2/m$) M06				
10	P_1–P_2	2.130	0.141	-0.272	4.506	-0.095	0.193	(3,-1)
	P_1–P_3	4.293						no bond
	Se_1–Se_2	3.456	0.014	0.030	0.945	0.000	0.516	(3,-1)
	Se_1–Se_3	3.492	0.013	0.028	0.947	0.000	0.515	(3,-1)
				HP-II ($P\bar{3}1m$) PBE0				
20	P_1–P_2	2.451	0.074	-0.014	2.165	-0.025	0.296	(3,-1)
	P_1–P_3	2.383	0.095	-0.082	2.970	-0.041	0.222	(3,-1)
	Se_1–Se_2	2.754	0.045	0.078	1.191	-0.005	0.534	(3,-1)
	Se_1–Se_3	3.162	0.024	0.049	1.105	-0.001	0.559	(3,-1)
				HP-II ($P\bar{3}1m$) M06				
20	P_1–P_2	2.480	0.070	-0.002	2.025	-0.022	0.310	(3,-1)
	P_1–P_3	2.449	0.082	-0.041	2.512	-0.031	0.245	(3,-1)
	Se_1–Se_2	2.829	0.039	0.077	1.107	-0.002	0.554	(3,-1)
	Se_1–Se_3	3.227	0.021	0.046	1.059	-0.001	0.571	(3,-1)